Thermal and mechanical characteristics of recycled concrete aggregates mixed with plastic wastes: experimental investigation and mathematical modeling

Ghorbani, Behnam, Yaghoubi, Ehsan and Arulrajah, Arul (2022) Thermal and mechanical characteristics of recycled concrete aggregates mixed with plastic wastes: experimental investigation and mathematical modeling. Acta Geotechnica, 17 (7). pp. 3017-3032. ISSN 1861-1125

Thermal and mechanical characteristics of recycled concrete aggregates mixed with plastic wastes: Experimental Investigation and Mathematical Modeling

Behnam Ghorbani[1], Ehsan Yaghoubi[1*], Arul Arulrajah[2]

Behnam Ghorbani[1]
Institute for Sustainable Industries and Liveable Cities, Victoria University, Melbourne, Australia. E-mail: behnam.ghorbani@vu.edu.au. ORCID ID: 0000-0002-8651-4402.

Ehsan Yaghoubi[1]
College of Engineering and Science, Victoria University, Melbourne, Australia. E-mail: ehsan.yaghoubi@vu.edu.au. ORCID ID: 0000-0003-0639-0225.

Arul Arulrajah[2]
Department of Civil and Construction Engineering, Swinburne University of Technology, Melbourne, Australia. E-mail: aarulrajah@swin.edu.au. ORCID ID: 0000-0003-1512-9803.

* Corresponding Author:

Ehsan Yaghoubi

Lecturer, College of Engineering & Science, Victoria University

Room D304, Level 3, Building D, Victoria University, Victoria 3011 Australia

E-mail: ehsan.yaghoubi@vu.edu.au

Telephone: +61 3 9919 4804

ABSTRACT

The growing rate of plastic waste generation is becoming a global concern due to the adverse impacts of plastics on the environment. Recycling and reusing plastic waste has been identified as a sustainable approach to mitigate the environmental concerns associated with landfilling of plastics. This study aims to evaluate the effect of the addition of waste polyethylene terephthalate (PET) on the thermal conductivity, resilient modulus, and strength properties of recycled concrete aggregate (RCA) as an alternative pavement construction material. A suite of laboratory tests including thermal conductivity, repeated load triaxial, unconfined compressive strength, and triaxial shear tests were undertaken to evaluate the effect of up to 10% waste PET on the performance of RCA as a pavement material. A relatively simple, yet robust, resilient modulus constitutive model was developed for RCA/PET blends using the multivariate adaptive regression spline (MARS) approach. The proposed model incorporated thermal conductivity, unconfined compressive strength, confining stress, and deviator stress for modeling the resilient modulus response of the RCA/PET blends. A unique feature of the developed model is the incorporation of thermal conductivity as model input. Several verification phases were conducted to validate the accuracy and reliability of the MARS model. The performance of the MARS model was compared with a neural network model to further evaluate the predictive capability of the developed model. The results indicated that the MARS model was an efficient and accurate tool in predicting the resilient modulus of recycled material blends. The experimental and numerical investigations aimed to provide novel insight into the thermal and mechanical properties of recycled materials to expand their usage in pavement and geotechnical applications.

Keywords: Thermal conductivity; Pavement geotechnics, Recycled waste materials; Waste plastic; Machine learning.

1. Introduction

The thermal conductivity of geo-materials is a key parameter in the design of energy geo-structures such as energy foundations, energy piles, shallow geothermal systems, and geothermal pavements [1-4]. Thermal conductivity controls the rate of heat flow in geo-materials and their responses under thermal loads. Knowledge of the thermal conductivity of geo-materials is essential for the understanding and analysis of heat transfer problems. Several transient and steady-state methods have been utilized for measuring the thermal conductivity of soils and rocks [1, 5, 6]. Divided bar [7, 8] is a reliable and accurate method that uses steady-state thermal equilibrium for determining thermal conductivity [9-11], and hence is used in the current study

Plastics have become an inseparable part of human lives due to their low cost, high durability, favorable physical and mechanical properties [12]. These merits have led to the rapid growth in production and use of plastics for household and industrial purposes. The increasing tendency in using plastics has gathered global attention recently, particularly due to the severe environmental consequences of plastic wastes. Plastics are non-biodegradable materials that are often destined to landfills. In Australia, approximately 2.5 million tons of plastic waste is produced annually, with a recycling rate of around 13% [13]. One sustainable alternative to landfilling is recycling or reusing waste plastics in high material-consuming industries, such as construction and earthworks. Accordingly, many researchers have attempted to investigate the reuse of several types of waste plastics, including polyethylene terephthalate (PET), high-density polyethylene, and low-density polyethylene plastics in civil engineering construction activities [14-17].

Construction and demolition (C&D) wastes have emerged as sustainable construction materials with numerous economic and environmental benefits [18]. Recycled concrete aggregate (RCA) is produced by the demolition of concrete structures and crushing concrete elements. RCA is the predominant stream of C&D materials that has superior strength and stiffness properties compared to other C&D types, such as crushed brick and waste excavation rock. RCA has been used in various civil engineering applications, particularly for the construction of pavement base and subbase layers [19, 20]. The favorable properties of RCA, such as high durability and resilient modulus comparable to high-quality virgin crushed rock make it a suitable candidate to be used in combination with other waste types with inferior mechanical properties.

Resilient modulus (*Mr*) is a fundamental material property that is being widely used in pavement design and analysis [21]. The most common approach for the determination of the *Mr* of pavement materials is by carrying out the repeated load triaxial (RLT) test. The RLT test simulates the response of pavement material under repeated loads of moving vehicles by applying various combinations of vertical and confining stresses to the sample. Several standards and specifications have been proposed for evaluating the *Mr* of unbound pavement materials [22-24]. Current specifications adopt varied loading magnitudes and pulse properties for determining the *Mr* of pavement base and subbase materials. The *Mr* of pavement base/subbase materials is affected by several parameters including aggregate characteristics, gradation, compaction characteristics, and applied stress levels [25-27]. While performing laboratory tests is one of the most accurate and reliable methods for determining the *Mr*, it is a time-consuming and costly procedure that requires advanced testing equipment and experienced laboratory operators. Therefore, several constitutive models have been proposed for the prediction of the *Mr* response of pavement materials. Such models include simple correlations with strength tests such as unconfined compressive strength (UCS) and California bearing ratio (CBR) [28], models incorporating stress-state parameters [29-31], and more advanced models incorporating a combination of physical properties, strength parameters, and stress state parameters [32-34].

In the last decades, advancements in computer software and hardware technology have led to novel methods for solving engineering problems. Machine learning methods are algorithm-based approaches that identify the trends and patterns in data. These algorithms are capable of extracting the knowledge from data quickly and do not require any prior assumption about the investigated problem. Machine learning methods have been applied for solving several problems in various fields of civil and geotechnical engineering, such as mechanical behavior of soils and recycled materials [26, 35, 36], permeability prediction of rocks [37, 38], and thermal conductivity of soils [39, 40]. In recent years, machine learning methods have been utilized for constitutive modeling of the *Mr* for pavement materials [41, 42]. While extensive research has been conducted on the laboratory characterization of C&D materials in transportation infrastructure applications, *Mr* constitutive modeling for C&D materials using machine learning methods is still lacking.

The current research study has two main objectives. The first objective is to investigate the effect of using waste PET on the thermal and mechanical properties of RCA as a widely accepted recycled pavement material. An extensive experimental study was conducted to evaluate the effect of plastic waste on the thermal conductivity, *Mr*, UCS, and shear strength (q_{peak}) of the RCA. The *Mr* of RCA/PET blends was examined in various ranges of confining and deviator stresses to understand their stiffness response under different loading conditions. The second objective of this research is to develop a mathematical expression between the *Mr* and thermal conductivity, UCS, confining stress, and deviator stress of RCA/PET blends using a robust machine learning method. This research explains how simple testing parameters such as UCS and unconventional material properties such as thermal conductivity can be used for *Mr* constitutive modeling of recycled materials. The outcomes of this research aim to advance the application of recycled materials in geotechnical and pavement structures by providing user-friendly, yet reliable numerical models backed up with robust laboratory test results.

2. Materials and methods

2.1. Experimental characterization

The materials used for experimental tests comprised RCA and waste PET. RCA was collected from a recycling site and PET was sourced by shredding the plastic bottles from the municipal waste stream in Victoria, Australia. RCA was blended with 1%, 3%, 5%, 7%, and 10% PET, by weight, to understand the effect of waste plastic on thermal and mechanical responses of RCA as the predominant type of demolition wastes. **Fig. 1** presents the particle size distribution of RCA and PET. RCA and PET were classified as well-graded gravel and poorly (or uniformly)-graded sand, respectively, according to the USCS classification system. The physical appearance and scanning electron microscopy images of materials are presented in **Fig. 2.** RCA had a uniform micro-structure with bulky-shaped aggregates while PET aggregates had lamellar and flaky shapes. **Fig. 3** shows the optimum moisture content (OMC), maximum dry density, and void ratio (*e*) of the blends at their maximum dry densities. The addition of PET increased both OMC and the void ratio. The increase in OMC could be due to the need for more moisture to facilitate the movements of PET particles for achieving the desired workability, and hence reaching the maximum dry density. The increase in the void ratio by adding a greater percentage of plastic particles could be because a portion of the compaction energy was absorbed by the PET particles, which influences the packing properties of the blends.

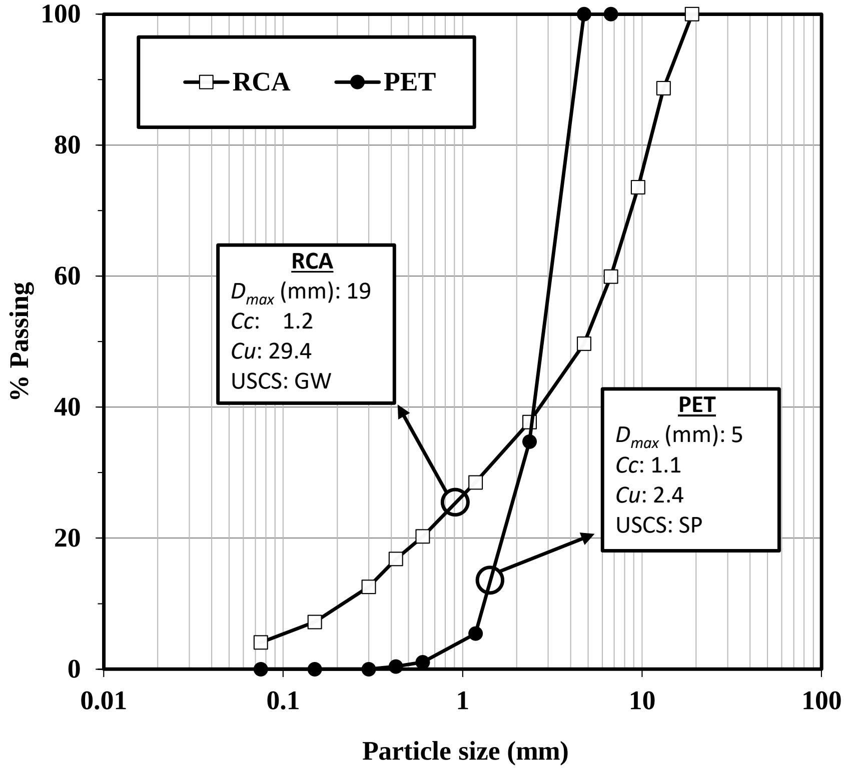

Fig. 1 Particle size distribution curves of RCA and PET

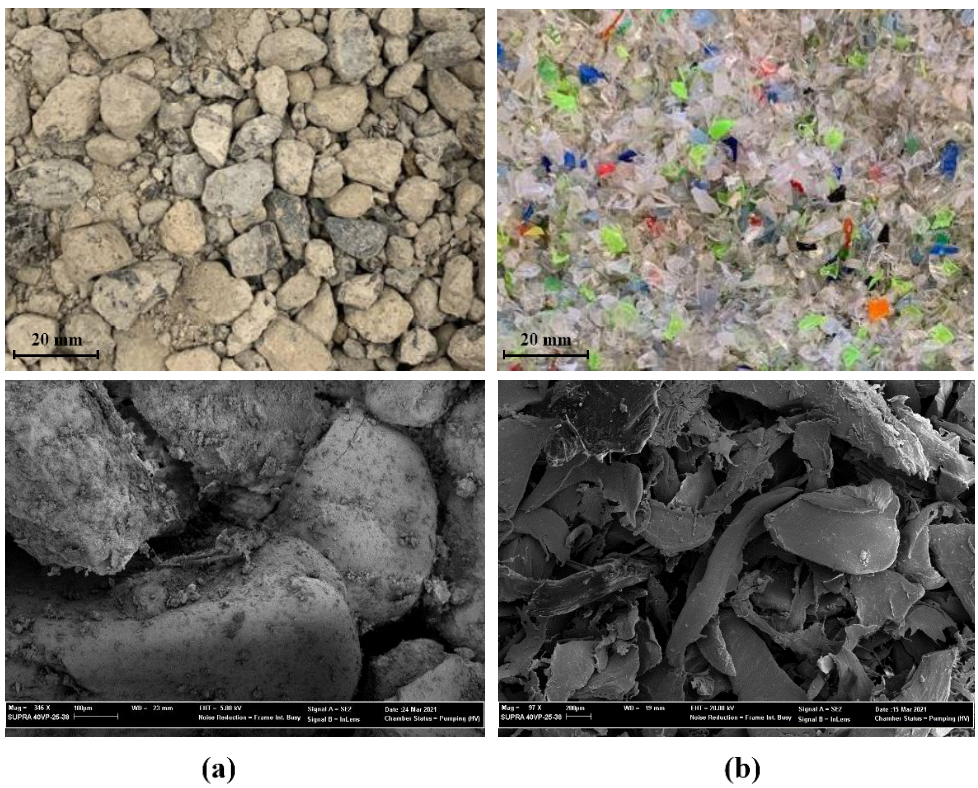

Fig. 2 SEM images and physical appearance of the materials: (a) RCA (b) PET

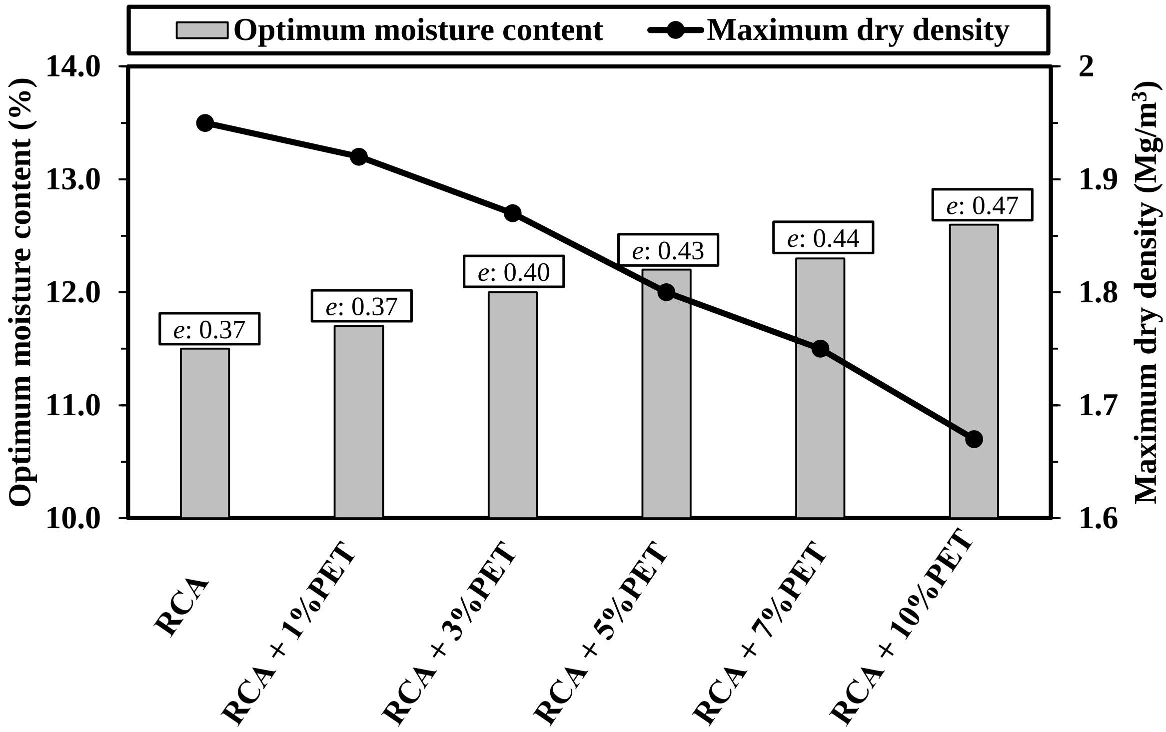

Fig. 3 Physical properties of the RCA/PET blends

The thermal conductivity of the RCA/PET blends was determined using the divided bar method. For this, cylindrical samples with the diameter and height of 100 mm and 50 mm, respectively, were prepared using the modified compaction energy as per ASTM D1557 [43]. The divided bar equipment is illustrated in **Fig. 4**. The apparatus comprised of copper disks with a standard material in between at both ends of the sample. Temperature sensors were inserted into the copper plates to monitor the temperature variations across the sample and the standard material. Constant temperatures were maintained on the top and bottom of the system using a temperature-controlled system. The thermal conductivity of the sample was obtained once the system reached steady-state thermal equilibrium, i.e., when no further variations in the logged temperatures were observed. The thermal conductivity of samples was determined at different PET contents and moisture levels.

Unconfined compressive strength (UCS) tests were carried out at a constant loading rate of 1 mm/min, to examine the effect of percentage of PET on the strength and stress-strain response of the RCA. The UCS samples were prepared in cylindrical molds with internal height and diameter of 115.5 mm and 105 mm, respectively, using the modified compaction energy [43].

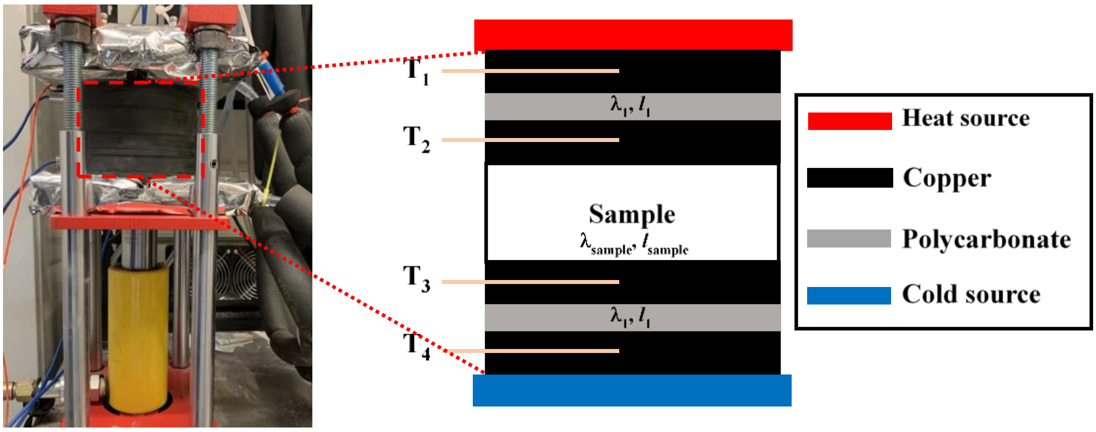

$$q_1 = q_2 = q_{sample}$$

$$\frac{\lambda_1.(T_2 - T_1)}{l_1} = \frac{\lambda_1.(T_3 - T_4)}{l_1} = \frac{\lambda_{sample}.(T_2 - T_3)}{l_{sample}}$$

$T_1 - T_4$: temperature sensors; q: heat flux; l: sample thickness; λ: thermal conductivity.

Fig. 4 Schematic presentation of the divide bar equipment

The *Mr* of blends was assessed according to the stress combinations summarized in **Table 1**, following a user-defined scheme by modifying the stress levels of AASHTO [22] and CEN EN 13286-7 [44]. The range of the adopted confining stress (σ_c) and deviator stress (σ_d) were 15 – 120 kPa and 35 – 410 kPa, respectively. Higher stress ratios (σ_d / σ_c) than 10 were applied in lower confinement levels to capture the response of the samples under extreme conditions. Lower stress ratios were applied to the sample in the initial stages, followed by more demanding stress ratios in subsequent stages. A harmonized loading approach similar to NCHRP 1-28A [23] was adopted in which the σ_c and σ_d increased simultaneously in each stage of the test, to avoid the failure of samples in the initial loading stages. After the completion of the repeated loading procedure, the shear strength of blends was determined in a constant σ_c of 40 kPa by applying a deformation rate of 1 mm/min.

Table 1 Stress combinations of the RLT test

Sequence	Contact stress, $0.2\sigma_c$	Confining stress, σ_c (kPa)	Deviator stress, σ_d (kPa)	Sequence	Contact stress, $0.2\sigma_c$	Confining stress, σ_c (kPa)	Deviator stress, σ_d (kPa)
Conditioning	20	100	80	18	12	60	205
1	3	15	35	19	16	80	245
2	6	30	65	20	20	100	280
3	9	45	90	21	24	120	300
4	12	60	115	22	3	15	125
5	16	80	145	23	6	30	170
6	20	100	170	24	9	45	210
7	24	120	190	25	12	60	250
8	3	15	65	26	16	80	295
9	6	30	100	27	20	100	335
10	9	45	130	28	24	120	355
11	12	60	160	29	3	15	155
12	16	80	195	30	6	30	205
13	20	100	225	31	9	45	250
14	24	120	245	32	12	60	295
15	3	15	95	33	16	80	345
16	6	30	135	34	20	100	390
17	9	45	170	35	24	120	410

2.2. Multivariate adaptive regression spline

Multivariate adaptive regression spline (MARS) is a nonparametric statistical approach proposed by Friedman [45]. MARS uses piecewise linear splines with different gradients for the function approximation. The main advantage of the MARS model lies in partitioning the data into small regions and fitting linear splines in each region, which gives it the flexibility to handle nonlinearities and complex interactions between variables/ high-dimensional problems [46, 47].

Two main components of the MARS algorithm are the knots and basis functions (BFs). A knot defines the location at which two splines with different slops coincide, and specifies the boundary between two regions of data [48, 49]. The resulting piecewise curves are referred to as BFs. The general form of the MARS model is as follows [45]:

$$f(x) = a_0 + \sum_{i=1}^{m} a_i BF_i\,(x) \tag{1}$$

where a_0 is the bias, a_i are the coefficients of the BFs, and BF_i (x) denote the basis function that can be a constant, hinge function, or the product of two or more hinge functions. The piecewise linear BFs of the MARS model can be defined as follows [45, 50]:

$$(x-t)_+ = \max(0, x-t) = \begin{cases} x-t & if\ x > t \\ 0 & otherwise \end{cases} \tag{2}$$

$$(t-x)_+ = \max(0, t-x) = \begin{cases} t-x & if\ x < t \\ 0 & otherwise \end{cases} \tag{3}$$

where t is the knot.

Fig. 5 presents a simple MARS model with two knots for fitting the synthetic data. The knots are located at x = 2.1 and x = 6.1. The mathematical expression of the MARS is expressed as:

$$\begin{aligned} &f(x) = -36.4 + 9.81 * BF1 + 9.9 * BF2 \\ &BF_1 = max(0, x - 2.1) \\ &BF_2 = max(0,6.1 - x) \end{aligned} \tag{4}$$

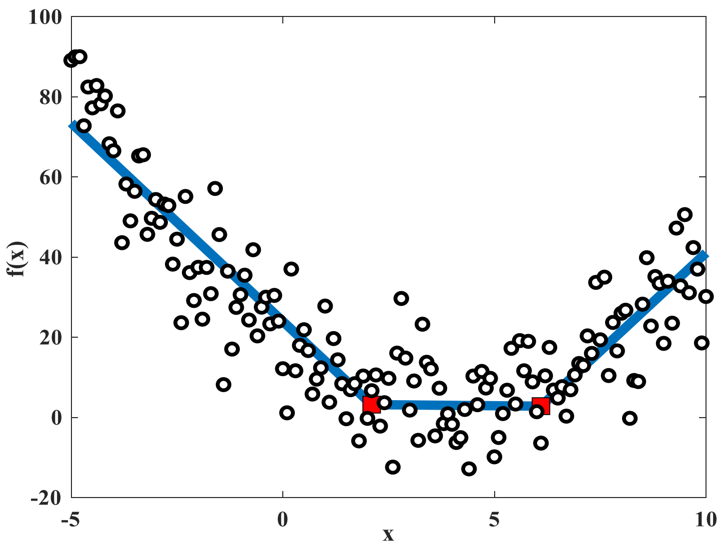

Fig. 5 A simple example of the MARS model for fitting the data

The MARS model development procedure initiates with the forward phase in which the knot locations and BFs are added to the model based on the minimization of the training error. This results in a model with a high probability of overfitting. In the second phase, a backward pruning algorithm is implemented to remove the BFs with the least contribution to the model [45, 47]. The performance of the model subsets are calculated and compared using generalized cross-validation (GCV), which makes a balance between the predictive capability and complexity of the developed model [45]:

$$GCV = \frac{\frac{1}{N}\sum_{i=1}^{N}[y_i - f(x_i)]^2}{\left[1 - \frac{m + d \times (m-1)/2}{N}\right]^2} \tag{5}$$

where N is the number of datasets, m is the number of BFs, and $f(x_i)$ denotes the predicted values by MARS. Further details on the MARS parameters can be found in Friedman [45].

3. Results and discussion

3.1. Experimental results

The thermal conductivity test results of RCA/PET blends using the divided bar method are summarized in **Table 2**. An increase in the thermal conductivity of the blends was observed as the moisture content increased. The increase rate of the thermal conductivity was greater in lower moisture contents and became slower in higher moisture contents close to the optimum moisture content. In the dry state, the voids are filled with air having low thermal conductivity (0.024 W/m.K). As the water content increased, a thin film was formed around the aggregates, in particular at contact points, and hence a further increase in the moisture content rapidly increased the thermal conductivity due to the higher thermal conductivity of water (0.598 W/m·K) compared to air. The increase in thermal conductivity was maintained at a slower rate as the sample reaches higher levels of saturation, possibly due to the fact that further addition of water had an insignificant effect on facilitating the heat transfer [1, 51, 52]. The thermal conductivity of RCA/PET blends tended to decrease when increasing the PET content. This decrease was attributed to the transition in the fabric of the sample from the RCA matrix to the RCA/PET matrix and the fact that PET particles exhibited low thermal conductivity values. The thermal conductivity of RCA varied between 1.14 – 1.69 W/m.K in the investigated moisture levels. On average, the thermal conductivity values for blends with 1%, 3%, 5%, 7%, and 10% PET decreased by approximately 5.5%, 12.5%, 20%, 27%, and 35% compared to those of pure RCA.

Table 2 Thermal conductivity of RCA/PET blends

Case	*w* (%)	λ (W/m.K)	Case	*w* (%)	λ (W/m.K)
RCA	13	1.692	RCA + 5%PET	13	1.383
	11	1.626		11	1.279
	9	1.430		9	1.143
	7	1.140		7	0.897
RCA + 1%PET	13	1.610	RCA + 7%PET	13	1.269
	11	1.520		11	1.180
	9	1.351		9	1.032
	7	1.075		7	0.831
RCA + 3%PET	13	1.525	RCA + 10%PET	13	1.106
	11	1.395		11	1.038
	9	1.248		9	0.931
	7	0.981		7	0.765

The stress-strain responses of the RCA/PET blends obtained from UCS tests are presented in **Fig. 6.** The addition of PET had a significant effect on the UCS values of the blends. The UCS values of the RCA containing 1% and 3% PET was 335 kPa and 263 kPa, respectively, which exhibited a reduction of approximately 13% and 32% compared to the UCS value of RCA. A closer look into **Fig. 6(a)** indicates that for RCA, the axial stress consistently increased with the axial strain up to the peak failure point and then dropped rapidly, indicating a relatively brittle response. The shape of the stress-strain graph considerably changed with the addition of PET and a significant increase in the ductility of the blends and reduction in the UCS values were noted when the PET content was more than 3%. The addition of 5%, 7%, and 10% PET resulted in a decrease of approximately 57%, 62%, and 82% in the UCS of RCA. The blends' axial strain at failure points and secant modulus at 50% of the UCS (E_{50}) are illustrated in **Fig. 6(b).** The E_{50} values were obtained using the Axial Stress- Axial Strain plots and by measuring the slope of the line drawn from the origin to the stress corresponding to half of the UCS peak. As evident, the addition of PET led to a rapid increase in the axial strain of the blends at failure and formed a monotonically-decreasing trend with E_{50}, indicating the enhanced ductility and reduced strength. This enhanced ductility can be attributed to the relatively smooth surface of PET in contrast to the rough surface of RCA which dominated the bearing capacity of the blends, particularly in higher PET contents [15].

The *Mr* is a key parameter in the design of pavement layers and provides information on the response of the material under various loading combinations. **Fig. 7** presents the *Mr* values of the RCA/PET blends obtained through the RLT testing. Increasing the confining and deviator stresses increased the *Mr* of blends. Higher confining stresses enhanced the interlock between the aggregates and increased the *Mr*. The stress-hardening response of the blends under the axial cyclic stresses also resulted in the increase of the *Mr*. **Fig. 7** also illustrates that the *Mr* of the blends was affected by the PET content, whereby inclusion of 1% PET reduced the *Mr* of the RCA by approximately 13%. This decrease in the *Mr* was maintained when increasing the PET content as the load-bearing mechanism of the blends was transferred from the rigid RCA aggregates to the PET contents. The *Mr* of the RCA was reduced to less than half once the PET content was more than 5%. This response can be related to the smooth surface, high compressibility, and lamellar shape of the PET particles that contribute to the reduction of inter-particle friction and consequently the stiffness of the blend [14, 15]. The recoverable strain (ε_r) and the *Mr* values are summarized in **Table 3**.

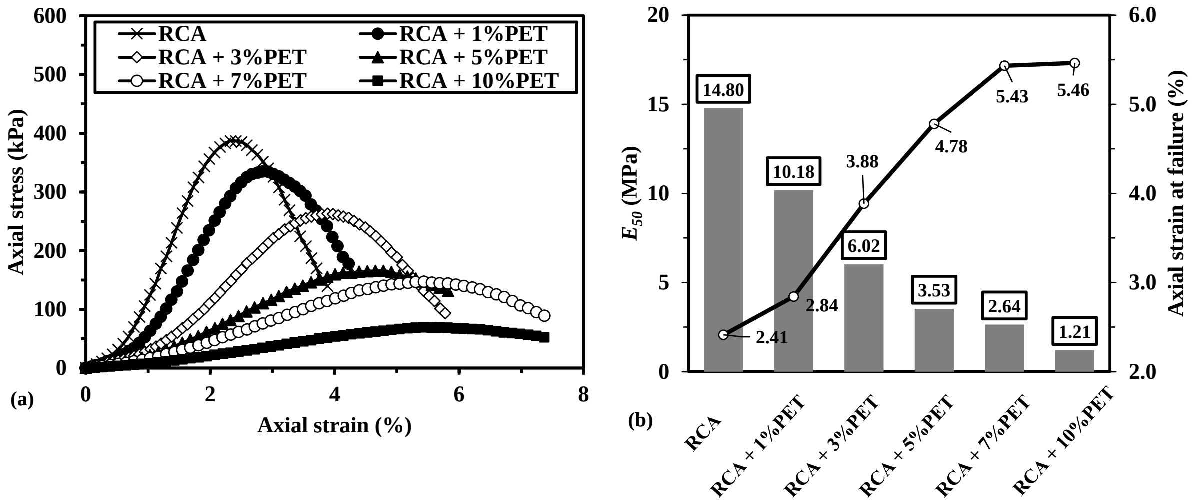

Fig. 6 Plots of (a) stress-strain response of the RCA/PET blends from UCS testing (b) E_{50} and axial strain at failure

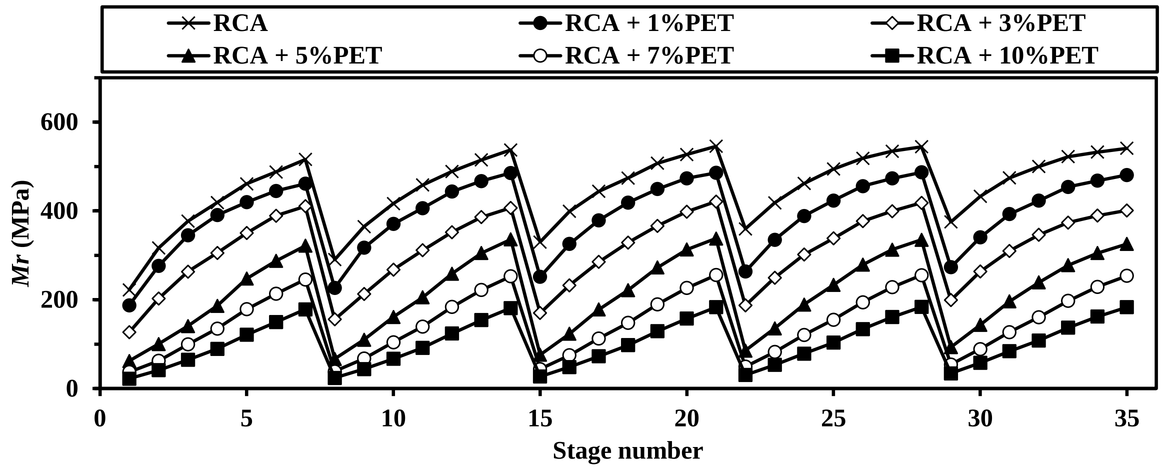

Fig. 7 *Mr* values of the RCA/PET blends

Fig. 8 shows the coupling effects of σ_c and σ_d on the *Mr* responses of the blends. One of the advantages of the adopted stress levels in **Table 1** was investigating the *Mr* of bends in high stress ratios at low confinement levels, which is the actual case in pavements. In **Fig. 8,** an evident drop was observed in the *Mr* when transitioning from 3% PET to 5%PET. This drop in the *Mr* values was more notable in results achieved under confining stress levels less than 45 kPa. These results highlight the effect of PET content on the *Mr* of RCA/PET blends which is more pronounced in low confinement levels. In addition, as the σ_c increased, the *Mr* values were less affected by the σ_d potentially due to the enhanced lateral support and hardening under applied cyclic loads.

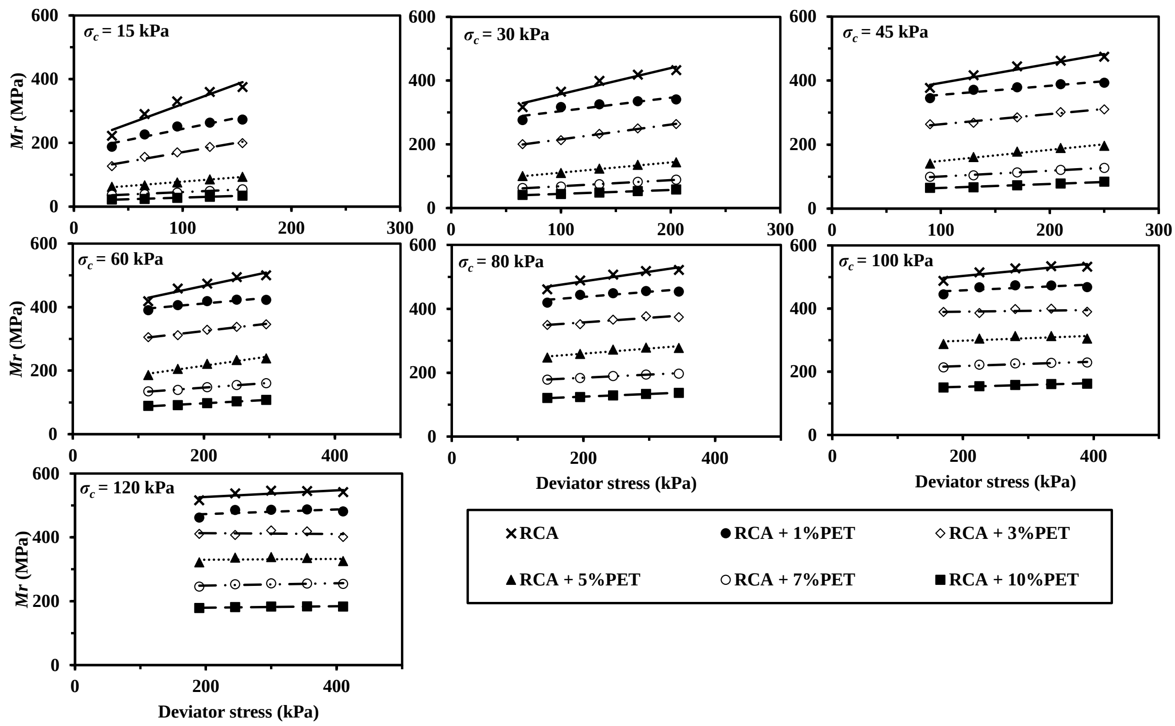

Fig. 8 The coupling effects of σ_c and σ_d on the *Mr*

Table 3. The ε_r and Mr values obtained from the RLT testing

	RCA		RCA + 1%PET		RCA + 3%PET		RCA + 5%PET		RCA + 7%PET		RCA + 10%PET	
Sequence	$\varepsilon_r \times 10^{-4}$	Mr (MPa)	$\varepsilon_r \times 10^{-4}$	Mr (MPa)	$\varepsilon_r \times 10^{-4}$	Mr (MPa)	$\varepsilon_r \times 10^{-4}$	Mr (MPa)	$\varepsilon_r \times 10^{-4}$	Mr (MPa)	$\varepsilon_r \times 10^{-4}$	Mr (MPa)
1	1.58	222.2	1.87	187.6	2.76	126.7	5.64	62.1	9.38	37.3	15.70	22.3
2	2.05	316.7	2.35	276.1	3.21	202.6	6.47	100.4	10.40	62.5	15.74	41.3
3	2.39	377	2.61	345.1	3.42	263.3	6.39	140.8	9.05	99.4	13.91	64.7
4	2.75	418.9	2.94	390.7	3.76	305.5	6.17	186.3	8.52	135	12.86	89.4
5	3.14	461.2	3.45	419.8	4.14	350.1	5.86	247.6	8.11	178.7	11.97	121.1
6	3.48	487.9	3.82	445.1	4.37	389.2	5.91	287.5	7.97	213.4	11.36	149.7
7	3.68	516.1	4.12	461.4	4.63	410.6	5.91	321.6	7.73	245.8	10.64	178.5
8	2.24	290.5	2.87	226.7	4.17	155.8	9.75	66.7	16.71	38.9	26.97	24.1
9	2.74	364.9	3.15	317.1	4.70	212.8	9.10	109.9	14.79	67.6	22.73	44
10	3.12	416.6	3.51	370.8	4.85	268	8.06	161.3	12.48	104.2	19.43	66.9
11	3.49	458.5	3.94	406.3	5.13	311.6	7.79	205.4	11.45	139.7	17.45	91.7
12	3.99	489.1	4.39	443.8	5.54	352.1	7.53	258.9	10.61	183.8	15.71	124.1
13	4.37	514.8	4.82	467.2	5.83	386.1	7.37	305.2	10.13	222.1	14.59	154.2
14	4.56	537.3	5.05	485.6	6.02	407	7.29	336.1	9.69	252.8	13.52	181.2
15	2.88	330.1	3.78	251.5	5.58	170.2	12.50	76	21.64	43.9	34.93	27.2
16	3.38	399.1	4.14	325.7	5.81	232.5	10.93	123.5	18.02	74.9	27.78	48.6
17	3.83	444.3	4.49	379	5.96	285.2	9.55	178	15.04	113	23.38	72.7
18	4.32	474.2	4.89	418.8	6.23	329	9.25	221.7	13.85	148	20.98	97.7
19	4.83	507.5	5.45	449.4	6.69	366.4	8.98	272.7	12.92	189.7	18.98	129.1
20	5.31	527.3	5.91	473.6	7.03	398.3	8.94	313.2	12.36	226.5	17.76	157.7
21	5.50	545.7	6.17	485.9	7.12	421.2	8.88	337.9	11.74	255.5	16.38	183.2
22	3.48	359.6	4.74	263.6	6.67	187.3	14.60	85.6	25.41	49.2	40.85	30.6
23	4.06	418.3	5.07	335.1	6.81	249.6	12.54	135.6	20.66	82.3	31.84	53.4
24	4.55	461.9	5.40	388.7	6.96	301.7	11.09	189.3	17.36	121	26.68	78.7
25	5.06	494.5	5.90	423.5	7.39	338.2	10.71	233.4	16.13	155	24.15	103.5
26	5.69	518.7	6.47	455.8	7.82	377.1	10.57	279.1	15.17	194.5	22.03	133.9
27	6.27	534.5	7.08	473.3	8.39	399.5	10.70	313	14.68	228.2	20.82	160.9
28	6.52	544.6	7.29	487	8.48	418.4	10.59	335.2	13.90	255.4	19.32	183.7
29	4.13	375.4	5.67	273.2	7.78	199.3	16.65	93.1	28.55	54.3	45.45	34.1
30	4.74	432.8	6.02	340.6	7.78	263.6	14.30	143.4	23.06	88.9	35.34	58
31	5.27	474.4	6.36	392.9	8.06	310.1	12.74	196.3	19.69	127	29.73	84.1
32	5.90	500.1	6.97	423.2	8.52	346.1	12.34	239	18.35	160.8	27.21	108.4
33	6.61	522.2	7.59	454.3	9.22	374	12.41	277.9	17.46	197.6	25.18	137
34	7.32	532.7	8.33	468.1	10.01	389.6	12.78	305.1	17.02	229.2	24.06	162.1
35	7.58	541.1	8.53	480.9	10.22	401.1	12.59	325.7	16.15	253.9	22.37	183.3

ε_r: recoverable strain, Mr: resilient modulus in MPa.

* Please refer to Table 1 for σ_c and σ_d values corresponding to each sequence of the RLT test.

The effect of PET on the shear strength (q_{peak}) and energy absorption capacity of the blends is presented in **Fig. 9**. The addition of 1%, 3%, 5%, 7%, and 10% of PET decreased the q_{peak} from 1050 kPa to 939 kPa, 759 kPa, 702 kPa, 654 kPa, and 608 kPa, resulting in approximately 11%, 28%, 33%, 37%, and 42% decrease in the q_{peak} due to the reduction in inter-particle friction. Despite the decrease in the strength and stiffness of the blends, the energy absorption capacity of the blends was enhanced with the addition of PET. The energy absorption capacity of the blends during the shear test was defined as the area under the stress-strain curve up to the peak shear strength as demonstrated in **Fig. 9**. The high compressibility and ductile fabric of the PET aggregates increased the energy absorption capacity of the blends. The increase in the energy absorption capacity was relatively rapid when the PET content was less than 3% and then became slower in higher PET contents.

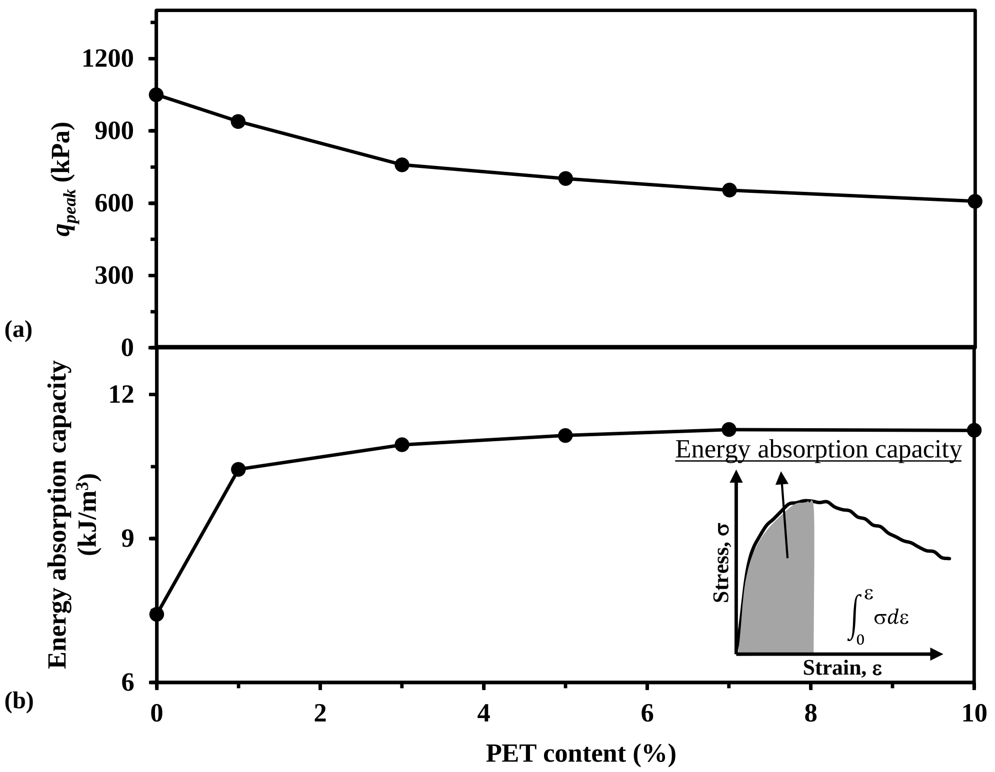

Fig. 9 (a) Shear strength (b) Energy absorption capacity of RCA/PET blends

The addition of PET to RCA resulted in the decrease in the UCS, *Mr*, and q_{peak}; however, with different rates, as illustrated in **Fig. 10**. In this figure, prepared following the approach undertaken by Gu et al. [53], *P* refers to the parameter in question (UCS, *Mr* or q_{peak}), P_0 is the parameter corresponding to the benchmark material (RCA) and P_n is the parameter corresponding to the blend with *n*% of PET. A closer inspection of the results reveals that q_{peak} decreased gradually with the increase in PET content, while the UCS and *Mr* exhibited a sharper drop. The q_{peak} value of the blends experienced initial drops of approximately 11% and an additional 17% with the addition of 1% and 3%PET, respectively, and then slightly reduced, emphasizing the beneficial effects of σ_c in higher PET contents under monotonic stress. Unlike the shear strength results, the UCS and *Mr* values decreased considerably with the increase in PET contents and both at relatively similar rates. Comparing the UCS and q_{peak} trends signifies the importance of σ_c on the strength properties of blends when PET is added to the RCA. The *Mr* of the blends was more affected by the variation of the PET content compared to the q_{peak}. This could be attributed to the repeated loading and unloading cycles which caused sudden particle movements due to the reduced surface friction at particles' contact points. The reduced shear strength as well as the increased ductility of the blends, i.e., higher recoverable strains, resulted in significant reductions in *Mr*.

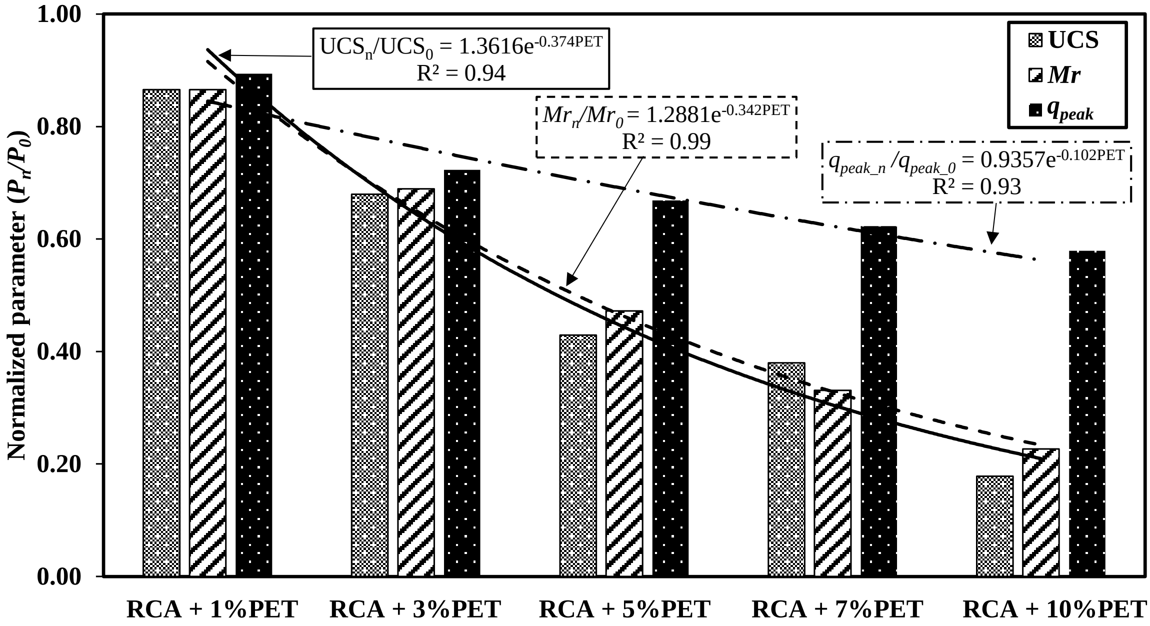

Fig. 10. Variations in the normalized strength and stiffness parameters with the PET content

MARS model development

Based on the results of the experimental tests, a multivariate adaptive regression spline model was developed for predicting the *Mr* of RCA/PET blends. The *Mr* of unbound pavement materials is generally obtained through empirical equations relating the *Mr* to stress state parameters through regression analysis. Some of the widely-used *Mr* constitutive models are summarized in **Table 4**. As noted in **Table 4**, such models have a predefined structure which might not represent the optimal structures of the investigated problem. In addition, a time-consuming regression analysis procedure is required to obtain the model coefficients. Herein, σ_c and σ_d were incorporated in the model as stress-state parameters. Both σ_c and σ_d have been found to be highly influential parameters on the *Mr* as evidenced in the experiments, *Mr* constitutive model, and the results reported in several studies [54-57]. These parameters were separately added to evaluate their independent impact on the Mr. In addition, UCS and λ were incorporated in the model as additional parameters to represent strength and physical properties of the blends. The parameter λ has been rarely used for developing *Mr* predictive models. Accordingly, it was believed that the combination of parameters adopted in the current study was suitable for developing a reliable *Mr* model.

Therefore, the *Mr* was formulated as a function of the thermal conductivity (λ) in W/m.K, UCS in kPa, confining stress (σ_c) in kPa, and deviator stress (σ_d) in kPa as follows:

$$Mr\ (MPa) = f(\lambda, UCS, \sigma_c, \sigma_d) \tag{6}$$

Table 4 General forms of *Mr* constitutive models

Reference	Model
Hicks [55]	$Mr = k_1 \left(\frac{\theta}{P_a}\right)^{k2}$
Puppala et al. [29]	$Mr = k_1 P_a \left(\frac{\sigma_c}{P_a}\right)^{k2} \left(\frac{\sigma_d}{P_a}\right)^{k3}$
Uzan [58]	$Mr = k_1 P_a \left(\frac{\theta}{P_a}\right)^{k2} \left(\frac{\sigma_d}{P_a}\right)^{k3}$
AASHTO [34]	$Mr = k_1 P_a \left(\frac{\theta}{P_a}\right)^{k2} \left(\frac{\tau_{oct}}{P_a} + 1\right)^{k3}$

θ: bulk stress, τ_{oct}: octahedral shear stress, P_a: atmospheric pressure, k_1-k_3: model coefficients

The database for model development comprised of 210 observations. One of the major concerns in the model development is overfitting. Overfitting occurs when the error of the model is low on the training data, however, the error values become large as new data is introduced to the model. To resolve this issue, it is suggested to divide the database into training and testing subsets before developing the model [11]. The database was randomly divided into training (80%) and testing (20%) subsets. A range of 15-30% of the data is typically taken for testing the machine learning algorithms [59-61]. The training subset (N_{train} = 168) was utilized for developing the MARS model, while the testing data (N_{test} = 42) was used to evaluate the predictive capability of the model on unseen data.

The performance of the developed model was assessed using statistical metrics including coefficient of determination (R^2), mean absolute error (MAE), and root mean square error (RMSE). The mathematical expressions of the statistical metrics are as follows:

$$R^2 = 1 - \frac{\sum_{i=1}^{n}(p_i - e_i)}{\sum_{i=1}^{n}(p - \bar{e})^2} \tag{7}$$

$$MAE = \frac{1}{n}\sum_{i=1}^{n}|p_i - e_i| \tag{8}$$

$$RMSE = \sqrt{\frac{\sum_{i=1}^{n}(p_i - e_i)^2}{n}} \tag{9}$$

where p_i and e_i are the predicted and experimental values of the i^{th} output, respectively, $\bar{e}$ is the average of experimental outputs, and n is the number of datasets. MAE measures the average of the residuals and gives equal weights to small and large errors, while RMSE gives higher weights to larger error values. The closer the R^2 value to 1 and the MAE and RMSE values to 0, the better the predictive capability of the developed model.

Table 5 summarizes the BFs of the MARS model. The optimal MARS model for predicting the *Mr* of RCA/PET blends consists of 9 BFs as follows:

$$\begin{aligned}\mathrm{Mr\ (MPa)} = 86.3\ &+ 0.414 * \mathrm{BF1}\ + 1.64 * \mathrm{BF2}\ - 2.61 * \mathrm{BF3}\ + 0.000465 \\ &* \mathrm{BF4}\ - 0.00259 * \mathrm{BF5}\ + 563 * \mathrm{BF6}\ - 174 * \mathrm{BF7}\ - 3.93 \\ &* \mathrm{BF8}\ + 5.71 * \mathrm{BF9}\end{aligned} \tag{10}$$

Table 5 BFs of the optimal MARS model

BF	Equation	BF	Equation
BF1	UCS	BF6	max(0, λ - 1.24)
BF2	max(0, σ_c - 60)	BF7	max(0, 1.24 - λ)
BF3	max(0, 60 - σ_c)	BF8	BF2 * max(0, λ - 1.35)
BF4	BF1 * max(0, σ_d -145)	BF9	BF3 * max(0, 1.35 - λ)
BF5	BF1 * max(0, 145 - σ_d)		

The importance of the input variables on the performance of the MARS model was evaluated using analysis of variance (ANOVA) decomposition. The results of the ANOVA decomposition of the MARS model are summarized in **Table 6**. The first column denotes the ANOVA function number and the last column presents the variables associated with the ANOVA function. The values of the GCV and R^2_{GCV} in the second and third columns of the table correspond to the MARS model with that function removed. A function with a larger GCV value and lower R^2_{GCV} value has a higher effect on the performance of the MARS model. As noted, σ_c had a higher impact on the *Mr* of RCA/PET blends compared to other contributing parameters. In addition to the ANOVA decomposition data presented in **Table 6**, the relative importance of the input variables on the Mr is illustrated in **Fig. 11**. The *Mr* of the RCA/PET blends was mostly affected by the σ_c and other input variables had relatively similar amount of influences, which coincided with the results presented in **Table 6**. This was in agreement with the experimental results which highlighted the beneficial effects of σ_c on the *Mr* and q_{peak} of the RCA/PET blends, as discussed in Section 3.1 regarding **Figure 10**.

Table 6 ANOVA decomposition of the MARS model

Function	GCV	R^2_{GCV}	Variable
1	161.331	0.993	UCS
2	370.885	0.983	λ
3	2035.354	0.908	σ_c
4	455.232	0.979	UCS, σ_d
5	268.033	0.988	λ, σ_c

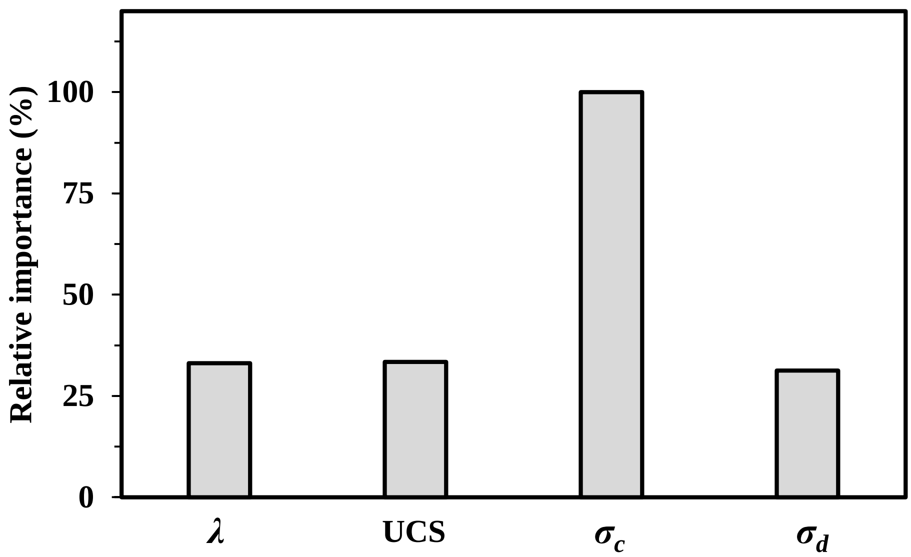

Fig. 11. The relative importance of the input variables on the *Mr*

Fig. 12 presents the predicted *Mr* values of the MARS model versus experimental values. For both training and testing data, a high coefficient of determination (R^2) of 0.99 was obtained. MAERMSE values for training data were 7.16 and 9.34, respectively. These values were 8.14 and 10.62, respectively, for testing data. The results exhibited the acceptable performance of the MARS model in predicting the *Mr* values. The close values of the statistical measures (R^2, MAE, and RMSE) for training and testing data show that the developed MARS model is well-trained and has a high level of predictive accuracy.

The advantage of the MARS model over other machine learning methods such as artificial neural networks (ANNs) is in its transparent structure and ability to provide a mathematical formulation as given in **Equation 10**. In spite of this, the predictive capability of the MARS model was compared with an ANN model to additionally evaluate the developed model. The ANN model was developed using the same datasets utilized for developing the MARS model. The accurate performance of the ANN models highly depends on the structure of the model and tuning parameters, such as the number of hidden layers, number of hidden neurons, and the activation function type. After constructing several models with different combinations of parameters, the ANN model with one hidden layer, 3 hidden neurons, and tan-sigmoid activation function was found to yield the best results. The statistical performance of the ANN model is summarized in **Table 7**. The comparison of the statistical metrics of the ANN (**Table 7**) and MARS methods (**Fig. 12**) showed that both models were highly efficient for predicting the *Mr*; however, the MARS model outperformed the ANN model on test data, indicating its superior performance for predicting unseen data. In addition, the capability of the MARS approach in providing relatively simple and easy to understand formulations without requiring any data scaling and normalization processes makes it a reliable and robust tool as reported in several studies [46, 62-64].

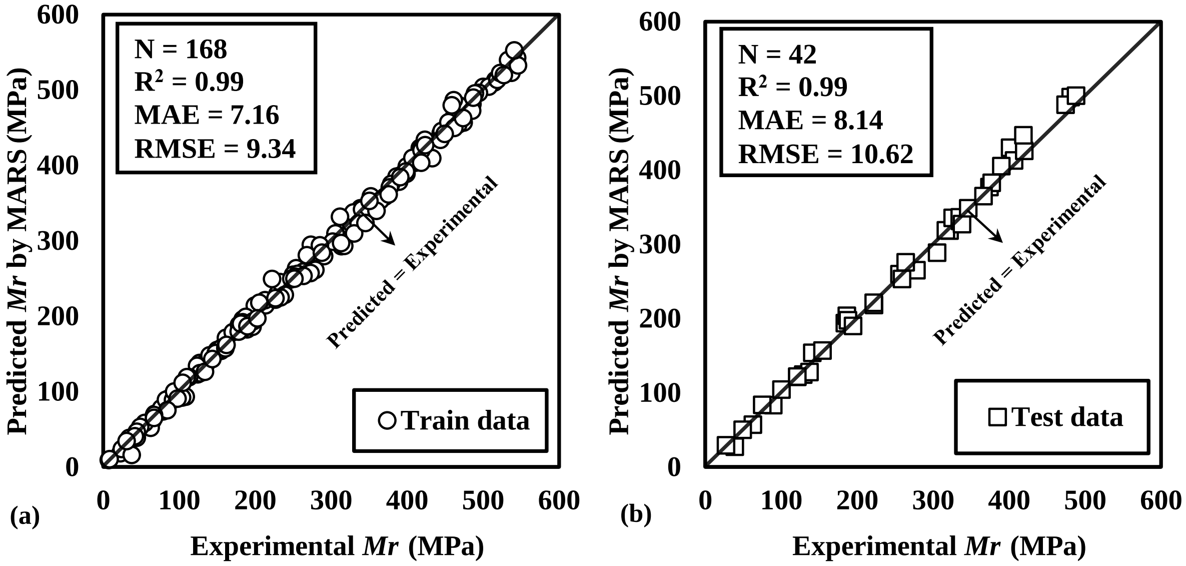

Fig. 12 Predicted values of the *Mr* by MARS model vs experimental values for (a) train data (b) test data

Table 7. Statistical evaluation of the ANN model

	R^2		MAE		RMSE	
	Train	Test	Train	Test	Train	Test
ANN model	0.99	0.99	6.45	10.47	9.19	15.25

To more accurately assess the error values of the MARS model for each dataset, the residual error (RE) was examined which is the difference between the experimental values and those predicted by the MARS model. Based on **Fig. 13**, the RE values were almost equally distributed on both sides of the horizontal axis. Approximately 95% of the datasets had RE values between -20 and 20, with a max |RE| value of 29.3.

The cumulative probability is another important indicator for evaluating the predictive performance of the model [65, 66]. **Fig. 14** presents the cumulative probability of the ratio of the predicted resilient modulus (Mr_P) and the experimental resilient modulus (Mr_E) for the test datasets. The $Mr_P/Mr_E = 1$ line which indicates the perfect prediction is also presented in this figure. It should be noted that $Mr_P/Mr_E > 1$ shows the over-prediction while $Mr_P/Mr_E < 1$ demonstrates the under-prediction. The values of the cumulative probabilities P_{50} and P_{90} for test datasets were 1.01 and 1.07, respectively, indicating the acceptable performance of the developed MARS model. While a few large erroneous values were observed, the trends of the error and statistical evaluation of the results demonstrated the acceptable and reliable performance of the developed model. The obtained errors for the MARS model (MAE, RMSE, and RE) were relatively small compared to the average *Mr* value of 269.9 MPa in the database. These results further verify the robustness of the MARS model for predicting the *Mr* values of RCA/PET blends.

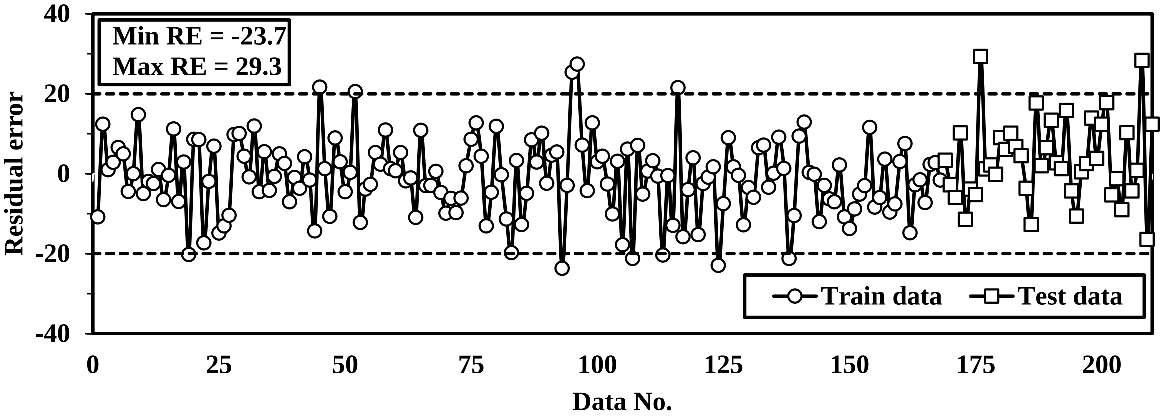

Fig. 13 Residual error values for training and testing data

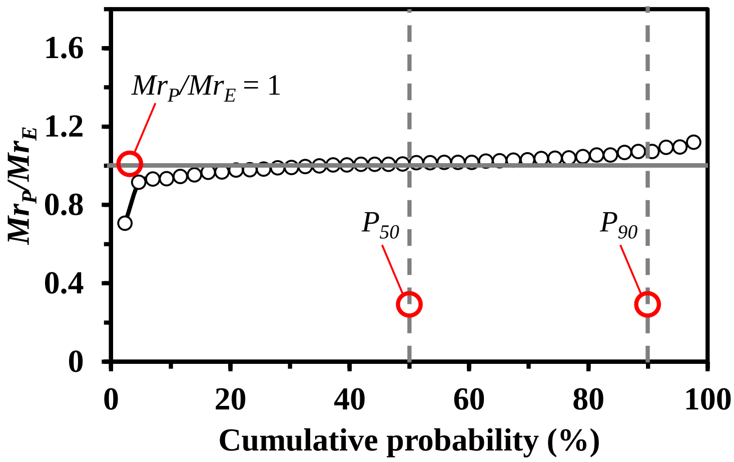

Fig. 14 The cumulative probability of Mr_P/Mr_E for testing datasets

Further to the above-mentioned validation methods, a parametric study was conducted to examine the responses of the MARS model to variations of input parameters. The parametric study evaluated the impact of the input variables on the *Mr* by varying each input variable over its range in the database. The results of the parametric study should match reasonably with experimental results to ensure the effectiveness of the MARS model. **Fig. 15** presents the response of the MARS model to variations in λ, UCS, σ_c, and σ_d. An increasing trend was observed in the *Mr* with increasing the UCS and λ. This was in agreement with experimental results which indicated that UCS and λ values were positively proportional to *Mr*. Increasing the PET content reduced the UCS and λ by decreasing the frictional resistance at particles' contact points and preventing proper heat transfer because of the low thermal conductivity of PET, respectively. An upward trend was also noted for the σ_c and σ_d due to the enhancement in the interlocking of aggregates stress hardening. It was also noted that the rise in the σ_d resulted in an increase in the *Mr* up to a point, after which σ_d had almost no impact on the *Mr*. This was because at high cyclic stresses values, samples were in the packed and densified state and increasing the cyclic stress had little influence on the *Mr*. The results of the parametric study were in agreement with the experimental results and the expected *Mr* behavior of recycled materials under the cyclic loads. This suggests that the MARS model was effective in capturing the response of variables and modeling the *Mr* of RCA/PET blends.

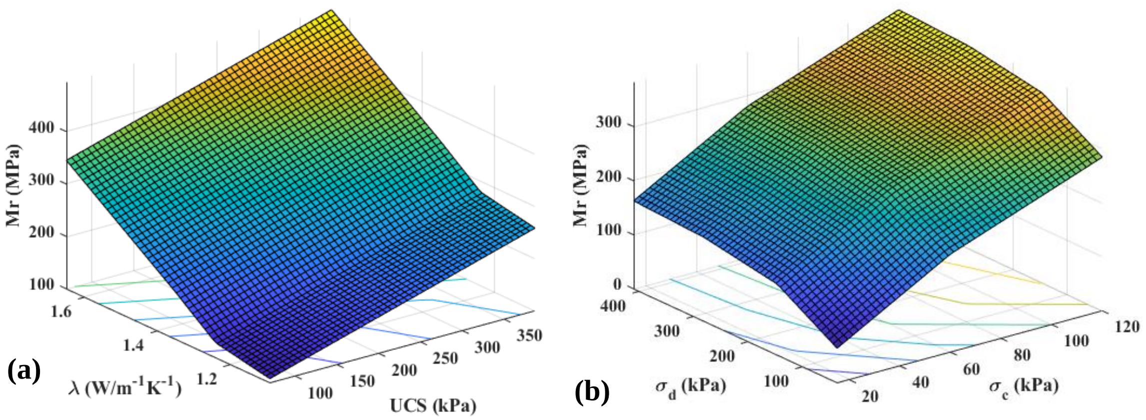

Fig. 15 The responses of the MARS model to variations in affecting parameters: (a) λ and UCS (b) σ_c and σ_d

4. Conclusions

This research investigated the effect of waste PET on the thermal and mechanical properties of RCA. A multivariate adaptive regression spline (MARS) model was developed for predicting the *Mr* of RCA/PET blends incorporating thermal conductivity, unconfined compressive strength, confining stress, and deviator stress as influential parameters. Based on the experimental and modeling results, the following conclusions can be drawn:

- The addition of PET reduced the thermal conductivity of RCA/PET blends. The reduction in thermal conductivity of the blends was attributed to the low thermal conductivity of PET particles as well as the increase in the void ratio of samples with increasing PET.
- The PET had considerable effects on the stiffness and strength properties of RCA. A sustained decreasing trend was observed in the *Mr*, UCS, and shear strength of the

samples as the PET content increased. Despite the detrimental effects of PET on the strength and stiffness properties of RCA, the energy absorption capacity of blends was improved with the addition of PET.

- The addition of recycled waste materials to unbound pavement layers has several environmental and economic benefits. It, however, may partially compromise the strength and stiffness properties of these materials. The UCS test results indicated an evident change in the stress-strain response at the PET content higher than 3%. In addition, the RLT test results indicated a sudden drop in the *Mr* of blends at lower confinement levels when the PET content transitioned from 3% to 5%. Therefore, 3%PET could be proposed as the optimum PET content in the unbound pavement layers, without compromising the functionality and stability of the pavement system, while maintaining a flexible response due to the energy absorption properties of plastic waste.
- The MARS approach was utilized for *Mr* constitutive modeling of the RCA/PET blends. The developed MARS model had excellent performance for predicting the *Mr*, with R^2 = 0.99 for both training and testing datasets.
- Several verification phases were implemented for evaluating the accuracy and reliability of the developed MARS model. The MARS model was found to be proficient in predicting the *Mr* and results were consistent with the underlying physical behavior of *Mr* in pavements.
- This study also highlights the capability of machine learning methods and their robustness for predicting the *Mr* of recycled materials. The developed MARS model can be readily used by researchers and practitioners for predicting the *Mr* of RCA/PET blends.

Declaration

Conflict of interest

The authors wish to confirm that there are no known conflicts of interest associated with this publication.

References

[1] D. Barry-Macaulay, A. Bouazza, R.M. Singh, B. Wang, P. Ranjith, Thermal conductivity of soils and rocks from the Melbourne (Australia) region, Engineering Geology 164 (2013) 131-138.

[2] Y. Xiao, B. Nan, J.S. McCartney, Thermal conductivity of sand–tire shred mixtures, Journal of Geotechnical and Geoenvironmental Engineering 145(11) (2019) 06019012.

[3] H.M. Abuel-Naga, D.T. Bergado, A. Bouazza, M.J. Pender, Thermal conductivity of soft Bangkok clay from laboratory and field measurements, Engineering Geology 105(3-4) (2009) 211-219.

[4] A. Arulrajah, B. Ghorbani, G. Narsilio, S. Horpibulsuk, M. Leong, Thermal performance of geothermal pavements constructed with demolition wastes, Geomechanics for Energy and the Environment (2021).

[5] N.H. Abu-Hamdeh, A.I. Khdair, R.C. Reeder, A comparison of two methods used to evaluate thermal conductivity for some soils, International Journal of Heat and Mass Transfer 44(5) (2001) 1073-1078.

[6] S. Roshankhah, A.V. Garcia, J. Carlos Santamarina, Thermal Conductivity of Sand–Silt Mixtures, Journal of Geotechnical and Geoenvironmental Engineering 147(2) (2021) 06020031.

[7] A. Benfield, Terrestrial heat flow in Great Britain, Proceedings of the Royal Society of London. Series A. Mathematical and Physical Sciences 173(955) (1939) 428-450.

[8] E.C. Bullard, Heat flow in south africa, Proceedings of the Royal Society of London. Series A. Mathematical and Physical Sciences 173(955) (1939) 474-502.

[9] A. Antriasian, G. Beardsmore, Longitudinal heat flow calorimetry: a method for measuring the heat capacity of rock specimens using a divided bar, Geotechnical testing journal 37(5) (2014) 859-868.

[10] J. Côté, J.-M. Konrad, Thermal conductivity of base-course materials, Canadian Geotechnical Journal 42(1) (2005) 61-78.

[11] B. Ghorbani, A. Arulrajah, G. Narsilio, M. Bo, Thermal and mechanical properties of demolition wastes in geothermal pavements by experimental and machine learning techniques, Construction and Building Materials 280 (2021).

[12] S. Wong, N. Ngadi, T.A.T. Abdullah, I.M. Inuwa, Current state and future prospects of plastic waste as source of fuel: A review, Renewable and sustainable energy reviews 50 (2015) 1167-1180.

[13] J. Pickin, P. Randell, Australian national waste report 2018, Department of the Environment and Energy (2018).

[14] B. Ghorbani, A. Arulrajah, G. Narsilio, S. Horpibulsuk, M.W. Bo, Shakedown analysis of PET blends with demolition waste as pavement base/subbase materials using experimental and neural network methods, Transportation Geotechnics (2021) 100481.

[15] E. Yaghoubi, A. Arulrajah, Y.C. Wong, S. Horpibulsuk, Stiffness properties of recycled concrete aggregate with polyethylene plastic granules in unbound pavement applications, Journal of Materials in Civil Engineering 29(4) (2016) 04016271.

[16] M. Dalhat, H. Al-Abdul Wahhab, K. Al-Adham, Recycled plastic waste asphalt concrete via mineral aggregate substitution and binder modification, Journal of Materials in Civil Engineering 31(8) (2019) 04019134.

[17] M. Belmokaddem, A. Mahi, Y. Senhadji, B.Y. Pekmezci, Mechanical and physical properties and morphology of concrete containing plastic waste as aggregate, Construction and Building Materials 257 (2020) 119559.

[18] P. Ghisellini, M. Ripa, S. Ulgiati, Exploring environmental and economic costs and benefits of a circular economy approach to the construction and demolition sector. A literature review, Journal of Cleaner Production 178 (2018) 618-643.
[19] A. Alnedawi, M.A. Rahman, Recycled concrete aggregate as alternative pavement materials: Experimental and parametric study, Journal of Transportation Engineering, Part B: Pavements 147(1) (2021) 04020076.
[20] A. Gabr, K. Mills, D. Cameron, Repeated load triaxial testing of recycled concrete aggregate for pavement base construction, Geotechnical and Geological Engineering 31(1) (2013) 119-132.
[21] D. Wang, M. Tawk, B. Indraratna, A. Heitor, C. Rujikiatkamjorn, A mixture of coal wash and fly ash as a pavement substructure material, Transportation Geotechnics 21 (2019) 100265.
[22] AASHTO, AASHTO T307, Determining the Resilient Modulus of Soils and Aggregate Materials, Standard Specifications for Transportation Materials and Methods of Sampling and Testing, Washington, D, C, 2003.
[23] NCHRP 1-28A, Laboratory determination of resilient modulus for flexible pavement design. , National Cooperative Highway Research Program Washington, D.C., United States, 2004.
[24] AustRoads, Determination of permanent deformation and resilient modulus characteristics of unbound granular materials under drained conditions, AustRoads Sydney, NSW, Australia, 2000.
[25] A. Ramos, A.G. Correia, B. Indraratna, T. Ngo, R. Calçada, P.A. Costa, Mechanistic-empirical permanent deformation models: Laboratory testing, modelling and ranking, Transportation Geotechnics (2020) 100326.
[26] B. Ghorbani, A. Arulrajah, G. Narsilio, S. Horpibulsuk, M.W. Bo, Dynamic characterization of recycled glass-recycled concrete blends using experimental analysis and artificial neural network modeling, Soil Dynamics and Earthquake Engineering 142 (2021) 106544.
[27] F. Lekarp, Resilient and permanent deformation behavior of unbound aggregates under repeated loading, Institutionen för infrastruktur och samhällsplanering, 1999.
[28] AASHTO, AASHTO guide for design of new rehabilitated pavement structures, (2002).
[29] A.J. Puppala, L.N. Mohammad, A. Allen, Engineering behavior of lime-treated Louisiana subgrade soil, Transportation Research Record 1546(1) (1996) 24-31.
[30] H. Seed, F. Mitry, C. Monismith, C. Chan, Prediction of flexible pavement deflections from laboratory repeated-load tests, NCHRP report (35) (1967).
[31] M. Witczak, J. Uzan, The universal airport pavement design system, Report I of V: granular material characterization, Department of Civil Engineering, University of Maryland, College Park, MD (1988).
[32] D.-G. Kim, Development of a constitutive model for resilient modulus of cohesive soils, The Ohio State University, 2004.
[33] N.C.H.R. Program, Guide for Mechanisticempirical Design of New and Rehabilitated Pavement Structures, 2004.
[34] AASHTO, Mechanistic-empirical pavement design guide: A manual of practice, AASHTO (2015).
[35] P. Zhang, Z.-Y. Yin, Y.-F. Jin, X.-F. Liu, Modelling the mechanical behaviour of soils using machine learning algorithms with explicit formulations, Acta Geotechnica (2021) 1-20.
[36] Z. Liu, J. Shao, W. Xu, Q. Wu, Indirect estimation of unconfined compressive strength of carbonate rocks using extreme learning machine, Acta Geotechnica 10(5) (2015) 651-663.
[37] N. Kardani, A. Bardhan, S. Gupta, P. Samui, M. Nazem, Y. Zhang, A. Zhou, Predicting permeability of tight carbonates using a hybrid machine learning approach of modified equilibrium optimizer and extreme learning machine, Acta Geotechnica (2021) 1-17.

[38] M. Tembely, A.M. AlSumaiti, W.S. Alameri, Machine and deep learning for estimating the permeability of complex carbonate rock from X-ray micro-computed tomography, Energy Reports 7 (2021) 1460-1472.
[39] W. Fei, G.A. Narsilio, M.M. Disfani, Predicting effective thermal conductivity in sands using an artificial neural network with multiscale microstructural parameters, International Journal of Heat and Mass Transfer 170 (2021) 120997.
[40] H. Karami, D. Robert, S. Costa, F. Tostovrsnik, B. O'donnell, S. Setunge, Construction of Working Platforms on Expansive Soils Using Recycled Concrete and Stabilizers: A Case Study, ICSECM 2019, Springer2021, pp. 19-30.
[41] X. Hu, P. Solanki, Predicting Resilient Modulus of Cementitiously Stabilized Subgrade Soils Using Neural Network, Support Vector Machine, and Gaussian Process Regression, International Journal of Geomechanics 21(6) (2021) 04021073.
[42] S. Hanandeh, A. Ardah, M. Abu-Farsakh, Using artificial neural network and genetics algorithm to estimate the resilient modulus for stabilized subgrade and propose new empirical formula, Transportation Geotechnics 24 (2020) 100358.
[43] ASTM D1557, Standard test methods for laboratory compaction characteristics of soil using modified effort, West Conshohocken, USA, 2012.
[44] CEN EN 13286-7, Unbound and hydraulically bound mixtures-part 7: cyclic load triaxial test for unbound mixtures, Brussels, 2004.
[45] J.H. Friedman, Multivariate adaptive regression splines, The annals of statistics (1991) 1-67.
[46] W. Zhang, A.T.C. Goh, Multivariate adaptive regression splines for analysis of geotechnical engineering systems, Computers and Geotechnics 48 (2013) 82-95.
[47] W. Zhang, R. Zhang, W. Wang, F. Zhang, A.T.C. Goh, A Multivariate Adaptive Regression Splines model for determining horizontal wall deflection envelope for braced excavations in clays, Tunnelling and Underground Space Technology 84 (2019) 461-471.
[48] W. Zhang, R. Zhang, C. Wu, A.T.C. Goh, S. Lacasse, Z. Liu, H. Liu, State-of-the-art review of soft computing applications in underground excavations, Geoscience Frontiers 11(4) (2020) 1095-1106.
[49] H. Zhou, H. Xu, X. Yu, Z. Guo, G. Zheng, X. Yang, Y. Tian, Evaluation of the bending failure of columns under an embankment loading, International Journal of Geomechanics 21(7) (2021) 04021112.
[50] T. Hastie, R. Tibshirani, J. Friedman, The elements of statistical learning: data mining, inference and prediction, Springer Series in Statistics2017.
[51] T. Zhang, G. Cai, S. Liu, A.J. Puppala, Investigation on thermal characteristics and prediction models of soils, International Journal of Heat and Mass Transfer 106 (2017) 1074-1086.
[52] L.A. Salomone, W.D. Kovacs, Thermal resistivity of soils, Journal of Geotechnical Engineering 110(3) (1984) 375-389.
[53] D. Gu, H. Liu, X. Gao, D. Huang, W. Zhang, Influence of Cyclic Wetting–Drying on the Shear Strength of Limestone with a Soft Interlayer, Rock Mechanics and Rock Engineering (2021) 1-10.
[54] T.V. Duong, Y.-J. Cui, A.M. Tang, J.-C. Dupla, J. Canou, N. Calon, A. Robinet, Effects of water and fines contents on the resilient modulus of the interlayer soil of railway substructure, Acta Geotechnica 11(1) (2016) 51-59.
[55] R.G. Hicks, Factors influencing the resilient properties of granular materials, University of California, Berkeley1970.
[56] F. Lekarp, U. Isacsson, A. Dawson, State of the art. I: Resilient response of unbound aggregates, Journal of transportation engineering 126(1) (2000) 66-75.

[57] A. Azam, D. Cameron, M. Rahman, Model for prediction of resilient modulus incorporating matric suction for recycled unbound granular materials, Canadian Geotechnical Journal 50(11) (2013) 1143-1158.
[58] J. Uzan, Characterization of granular material, Transportation research record 1022(1) (1985) 52-59.
[59] A.T. Goh, W. Zhang, An improvement to MLR model for predicting liquefaction-induced lateral spread using multivariate adaptive regression splines, Engineering geology 170 (2014) 1-10.
[60] A. Bardhan, C. Gokceoglu, A. Burman, P. Samui, P.G. Asteris, Efficient computational techniques for predicting the California bearing ratio of soil in soaked conditions, Engineering Geology (2021) 106239.
[61] Q. Ren, L. Ding, X. Dai, Z. Jiang, G. De Schutter, Prediction of Compressive Strength of Concrete with Manufactured Sand by Ensemble Classification and Regression Tree Method, Journal of Materials in Civil Engineering 33(7) (2021) 04021135.
[62] W. Zhang, A.T. Goh, Y. Zhang, Y. Chen, Y. Xiao, Assessment of soil liquefaction based on capacity energy concept and multivariate adaptive regression splines, Engineering Geology 188 (2015) 29-37.
[63] W. Zhang, A.T. Goh, Multivariate adaptive regression splines and neural network models for prediction of pile drivability, Geoscience Frontiers 7(1) (2016) 45-52.
[64] X. Qi, H. Wang, X. Pan, J. Chu, K. Chiam, Prediction of interfaces of geological formations using the multivariate adaptive regression spline method, Underground Space 6(3) (2021) 252-266.
[65] G. Zheng, W. Zhang, W. Zhang, H. Zhou, P. Yang, Neural network and support vector machine models for the prediction of the liquefaction-induced uplift displacement of tunnels, Underground Space 6(2) (2021) 126-133.
[66] M.Y. Abu-Farsakh, H.H. Titi, Assessment of direct cone penetration test methods for predicting the ultimate capacity of friction driven piles, Journal of Geotechnical and Geoenvironmental Engineering 130(9) (2004) 935-944.

LIST OF FIGURES

LIST OF TABLES